

Simple Replacement Reaction for the Preparation of Ternary $\text{Fe}_{1-x}\text{PtRu}_x$ Nanocrystals with Superior Catalytic Activity in Methanol Oxidation Reaction

Di-Yan Wang,[†] Hung-Lung Chou,[‡] Yen-Chen Lin,[†] Feng-Ju Lai,[§] Ching-Hsiang Chen,[§] Jyh-Fu Lee,^{||} Bing-Joe Hwang,^{*,§,||} and Chia-Chun Chen^{*,†,⊥}

[†]Department of Chemistry, National Taiwan Normal University, Taipei 116, Taiwan

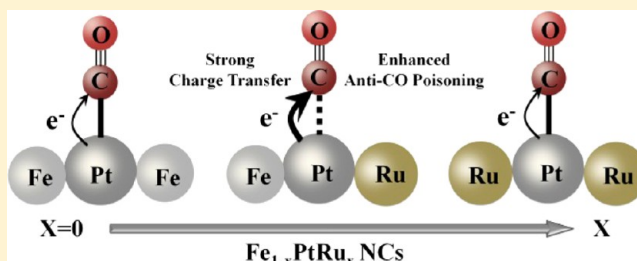
[‡]Graduate Institute of Applied Science and Technology, and [§]Nanoelectrochemistry Laboratory, Department of Chemical Engineering, National Taiwan University of Science and Technology, 106, Taiwan

^{||}National Synchrotron Radiation Research Center (NSRRC), Hsinchu 300, Taiwan

[⊥]Institute of Atomic and Molecular Science, Academia Sinica, Taipei 115, Taiwan

S Supporting Information

ABSTRACT: The finding of new metal alloyed nanocrystals (NCs) with high catalytic activity and low cost to replace PtRu NCs is a critical step toward the commercialization of fuel cells. In this work, a simple cation replacement reaction was utilized to synthesize a new type of ternary $\text{Fe}_{1-x}\text{PtRu}_x$ NCs from binary FePt NCs. The detailed structural transformation from binary FePt NCs to ternary $\text{Fe}_{1-x}\text{PtRu}_x$ NCs was analyzed by X-ray absorption spectroscopy (XAS). Ternary $\text{Fe}_{35}\text{Pt}_{40}\text{Ru}_{25}$, $\text{Fe}_{31}\text{Pt}_{40}\text{Ru}_{29}$, and $\text{Fe}_{17}\text{Pt}_{40}\text{Ru}_{43}$ NCs exhibit superior catalytic ability to withstand CO poisoning in methanol oxidation reaction (MOR) than do binary NCs (FePt and J-M PtRu). Also, the $\text{Fe}_{31}\text{Pt}_{40}\text{Ru}_{29}$ NCs had the highest alloying extent and the lowest onset potential among the ternary NCs. Furthermore, the origin for the superior CO resistance of ternary $\text{Fe}_{1-x}\text{PtRu}_x$ NCs was investigated by determining the adsorption energy of CO on the NCs' surfaces and the charge transfer from Fe/Ru to Pt using a simulation based on density functional theory. The simulation results suggested that by introducing a new metal into binary PtRu/PtFe NCs, the anti-CO poisoning ability of ternary $\text{Fe}_{1-x}\text{PtRu}_x$ NCs was greatly enhanced because the bonding of CO–Pt on the NCs' surface was weakened. Overall, our experimental and simulation results have indicated a simple route for the discovery of new metal alloyed catalysts with superior anti-CO poisoning ability and low usage of Pt and Ru for fuel cell applications.



1. INTRODUCTION

The search for anodic catalysts with high electrocatalytic activity in direct methanol fuel cells (DMFCs) has been ongoing in recent years.^{1–3} Binary catalysts based on PtRu alloy nanocrystals (NCs) have been recognized as being more efficient electrocatalysts for the methanol oxidation reaction (MOR) in comparison to pure Pt.^{4–10} Two main issues were considered in the search for new catalysts to replace Pt and/or Ru metal in DMFCs. First, the performance of the anode catalyst toward methanol oxidation and CO-tolerance had to be improved, and second, as both Pt and Ru are expensive, a cheaper metal replacement was sought. Recently, some transition metals have been incorporated into the PtRu system to form ternary alloy NCs.^{11,12} Ternary alloy NCs such as PtRuOs,¹³ PtRuW,¹⁴ PtRuMo,¹⁵ PtRuNi,¹⁶ PtRuSn,^{17,18} PtRuRh,¹⁹ and PtRuIr^{20–22} have demonstrated the advantages in catalytic activities with the addition of a new metal into PtRu NC. Some models were proposed to account for the catalytic activity enhancement for MOR. For examples, ternary PtRuMo

and PtRuW catalysts showed the transfer phenomenon of hydrogen ions in the Mo or W oxides for enhancing catalytic activity of methanol oxidation.^{14,15} The improved CO-tolerance of the PtRuNi NCs is related to the hydrogen spillover, which can liberate the Pt active sites due to transfer of hydrogen from Pt to Ni for enhancing the adsorption of methanol molecules on the catalyst's surface.¹⁶ PtRuSn NCs have demonstrated a higher catalytic activity than PtRu, due to the synergic effect of Ru as a water activator and Sn as an electronic modifier.²³ Those models have indicated that the catalytic activity enhancement might be reached by altering the electronic properties of Pt or Ru. However, few previous works have studied a series of the ternary NCs with different compositions and alloying extents to investigate the origins of the enhancements. Also, the systematical analyses of the structural and electronic properties of the ternary NCs by X-ray

Received: February 2, 2012

Published: May 30, 2012

absorption spectroscopy and theoretical modeling are still lacking.

Several studies have demonstrated that the catalytic activity of binary and ternary metal NCs increases with an increase in the alloying extent.^{24–27} This activity increase is mainly attributed to an increase in heteroatomic interactions.²⁸ In PtRu, the oxidation of CO on Pt depends on the distance between the Pt and Ru sites.^{29–32} PtRu NCs with a higher alloying extent have more heteroatomic interactions that lead to a higher catalytic activity for CO oxidation in comparison to the activity found in pure Pt or Ru systems.³³ Also, in PtRuIr systems, a catalytic mechanism has been proposed in which the addition of a 5d metal (Ir) in close proximity to Pt in the ternary NCs results in enhanced activity.³⁴ Here, the role of Ir is to promote methanol adsorption on Pt sites while accelerating the activation of MeOH C–H bonds. It is suggested that the alloying extent in the ternary NCs is a significant factor determining the catalytic activity enhancement of the NCs. Therefore, it is of importance to gain insight into the alloying of binary and ternary NCs.

As the extent of alloying is increased, heteroatomic interactions also increase; thus, heteroatomic interactions in the NCs are enhanced and lead to the change in the electronic environment of the metal atoms and an increase in catalytic activity.²⁸ For example, alloying extent studies of PtRu NCs by X-ray absorption spectroscopy (XAS) have indicated that the commercial binary PtRu catalyst (J-M 30) with a high alloying extent showed better specific electrocatalytic activity for MOR and lower onset potential for CO stripping than did E-TEK 30, which has a lower degree of alloying.³⁵ Other binary metal NCs (PtFe,³⁶ PtCo,³⁷ PtCr,³⁸ etc.) have shown that the catalytic activities of the binary NCs are strongly dependent on their alloying extent. Several synthesis strategies have been developed to control the NCs' alloying extent.^{39–41} The most commonly used method to tune the alloying extent is to change the atomic compositions used to form the NCs.⁴² However, during the formation process, identical atoms in the NCs aggregate to form small clusters, thereby resulting in a decrease in alloying.⁴³ Recently, synthetic strategies, for example, thermal annealing, have been used to improve the alloying extent of NCs.⁴⁴ This process promotes atomic segregation, thereby resulting in an increase in the extent of alloying. Also, chemical dealloying has been used to tune the alloying extent through acid treatment.⁴⁵ However, when the alloyed NCs are immersed in acid solution, the 3d metal and Pt atoms of the NCs dissolve, resulting in the NCs' collapse. Therefore, developing a facile synthetic strategy to manipulate the alloying extent, of binary or ternary NCs, is a prerequisite for improving catalytic activity.

Previously, ternary Fe_{1–x}PtRu_x NCs were synthesized from binary FePt NCs, and the chemical transformation from the binary to ternary NCs was characterized by XAS.¹² In this Article, a series of ternary Fe_{1–x}PtRu_x NCs with different alloying extents were prepared by a simple cation replacement reaction. The sizes, structures, compositions, and alloying extent of the NCs were measured by high-resolution transmission electron microscopy (HRTEM), powder X-ray diffraction (XRD), near-edge X-ray absorption spectroscopy (XANES), and extended X-ray absorption fine structure (EXAFS). The catalytic activities of the ternary Fe_{1–x}PtRu_x with different alloying extents, binary Fe₅₈Pt₄₂, and J-M PtRu NCs in the MOR were compared by linear sweep voltammograms and by determining their resistance to CO poisoning. A

simulation based on density function theory was used to calculate the CO adsorption energy and transfer charge of pure Pt, binary, and ternary NCs. A model was developed to shed light on the origin of the CO poisoning resistance ability of the ternary NCs when used for the MOR based on the experimental measurements and theoretical calculations. Our results showed that Fe_{1–x}PtRu_x NCs provided great advantage of lower usage of expensive Pt and Ru metals as well as enhanced the anti-CO poisoning ability on MOR.

2. EXPERIMENTAL SECTION

Chemicals. Platinum(II) acetylacetonate (99%), iron pentacarbonyl (98%), oleic acid (90%), and oleyl amine (80%) were purchased from Acros. 1,2-Hexadecanediol (90%) and dioctylether (99%) were purchased from Aldrich. Ruthenium(III) chloride (99%) was purchased from Alfa Aesar. All chemicals were used as received.

Synthesis of Binary FePt NCs. First, Pt(acac)₂ (95 mg) and 1,2-hexadecanediol (195 mg) were weighed, and then 10 mL of dioctyl ether was added into the three-necked flask. The solution temperature was kept at 100 °C for 15 min. While the reaction mixture was vigorously stirred, oleylamine (0.08 mL), oleic acid (0.08 mL), and Fe(CO)₅ (0.06 mL) were injected by syringe into the solution, which was heated to the boiling point of dioctyl ether, 300 °C. After being refluxed for 30 min, the heating mantle was removed, and the mixture was cooled to room temperature. Ethanol (20 mL) was added to the reaction mixture, which was separated by centrifuging. After centrifugation, a black precipitate was obtained. The products were redissolved in toluene.

Synthesis of Ternary Fe_{1–x}PtRu_x NCs. The binary FePt nanocrystal solution in toluene (10 mL) was mixed with an ethanolic solution of RuCl₃ (1 mL, 10 mM). The resulting solution was heated and stirred at 85 °C for 3, 10, or 15 h. The resulting solutions were centrifuged, and the black precipitates were collected and washed with a large amount of ethanol several times to remove any remaining metallic salts. The ternary Fe_{1–x}PtRu_x NCs ($x = 25, 29$, and 43) were prepared by a cation redox reaction.

Preparation of Carbon-Supported Binary FePt and Ternary Fe_{1–x}PtRu_x NCs. We added Vulcan XC-72 carbon (40 mg) into 10 mg each of the FePt and Fe_{1–x}PtRu_x NCs in toluene for ultrasonication overnight, respectively. We added ethanol (20 mL) to the reaction mixture, which was then separated by centrifugation. After centrifugation, carbon-supported binary FePt and ternary Fe_{1–x}PtRu_x NCs (i.e., FePt/C NCs and Fe_{1–x}PtRu_x/C NCs) were obtained.

Heat Treatment Procedure. All of the FePt/C and the Fe_{1–x}PtRu_x/C systems were subjected to a heat treatment step with the following procedure. The required quantity of each sample was taken up in a sample vial, and the system was purged with H₂ gas. The temperature was raised to 300 °C and kept at this temperature for 75 min to reduce the surface oxide and to eliminate the organic surfactant. After the thermal annealing treatment, the catalysts were further analyzed by X-ray absorption spectra, and their electrocatalytic activity was measured.

Powder X-ray Diffraction. XRD measurements were performed by Bruker D8 tools advance, operating with Cu K α radiation ($\lambda = 1.5406$ Å) generated at 40 keV and 40 mA. Scans were done at 0.01 ° for 2θ values between 30° and 90°.

Transmission Electron Microscopy (TEM). High-resolution TEM (HRTEM) measurements were performed with a Philips Technai G2 (FEI-TEM) microscope operating at 200 kV. The samples for the TEM analysis were prepared by ultrasonically dispersing the Fe_{1–x}PtRu_x NCs in toluene. A drop of the suspension was applied onto a carbon-coated copper grid and then dried in air.

X-ray Absorption Spectra (XAS) Measurements. The X-ray absorption spectra at the Fe K-edge and the Pt LIII-edge were recorded at the beamline 17C of the National Synchrotron Radiation Research Center (NSRRC) at Hsinchu, Taiwan. Ru K-edge was recorded at beamline 01C. The electron storage ring was operated at 1.5 GeV. Si(111) double crystal monochromator was utilized for data

collection by carrying out in the transmission mode. All of the spectra were collected at room temperature. For performing energy calibration, standard compounds, Pt foil, Ru powder, and Fe foil for the respective edges were measured simultaneously by using the third ionization chamber. The beam size was limited by the horizontal and vertical slits with the area of $2 \times 2 \text{ mm}^2$ during XAS measurements.

XAS Data Analysis. Standard procedures were followed to analyze the EXAFS data. First, in the pre-edge region, the raw absorption spectrum and the background above the edge were fitted to a straight line and using a 11-knot cubic spline function calculated from AUTOBK code, respectively. The EXAFS function, χ , was obtained by subtracting the postedge background from the overall absorption and then normalizing with respect to the edge jump step. To compensate for dampening of the XAFS amplitude with increasing k , the normalized $\chi(E)$ was transformed from energy space to k -space. The $\chi(k)$ data were weighted by k^3 . Subsequently, k^3 -weighted $\chi(k)$ data in the k -space ranging from 3.51 to 10.45 \AA^{-1} for Fe K-edge, from 3.58 to 13.07 \AA^{-1} for Pt LIII-edge, and from 4.1 to 13.5 \AA^{-1} for Ru K-edge were Fourier transformed (FT) to r -space to separate the EXAFS contributions from different coordination shells. A nonlinear least-squares algorithm was applied to curve fitting of EXAFS in r -space between 1.1 and 3.2 \AA for Fe K-edge, between 1.5 and 3.2 \AA for Pt LIII-edge, and between 1.3 and 3.3 \AA for the Ru K-edge (without phase correction) depending on the bond to be fitted. All of the computer programs were implemented in the UWXAFS 3.0 package⁴⁶ with the backscattering amplitude and the theoretically phase shift for the specific atom pairs being calculated by using Feff7 code. The references, iron foil, platinum foil, and ruthenium powder were employed for the Fe–Fe, Pt–Pt, and Ru–Ru bonds. On the basis of a face-centered cubic (fcc) model, Fe–Pt, Pt–Fe, and Ru–Fe bonds were modeled. By analyzing the Fe foil, Pt foil, and Ru powder, respectively, and by fixing the coordination numbers in the FEFFIT iNCut file, the amplitude reduction factor S_0^2 value for Fe, Pt, and Ru was obtained. The S_0^2 values were found to be 0.74, 0.91, and 0.84 for Fe, Pt, and Ru, respectively.

Electrode Preparation and Electrochemical Measurements. Millipore water (18 M Ω) and sulfuric acid (Across) were used in this study. All of the experiments were carried out at ambient temperature of $25 \pm 1^\circ\text{C}$, unless stated otherwise. A conventional three-electrode electrochemical cell was used for the CV measurements, with a high surface area Pt counter electrode and the saturated calomel electrode (SCE) reference (all potentials in this Article are quoted versus the RHE electrode), powered by a Solartron 1480 potentiostat/galvanostat. The working electrode was made of the commercial PtRu/C (J-M), FePt/C, and Fe_{1-x}PtRu_x/C catalysts immobilized on the GCE surface (0.1964 cm² area). The procedure for electrode fabrication involved three steps: first, the preparation of a clear suspension by sonicating a known amount of PtRu/C (J-M) and FePt/C and the Fe_{1-x}PtRu_x/C dispersed in 0.5% Nafion; second, placing an aliquot of the suspension (7 μL of 6.2 $\mu\text{g-Pt mL}^{-1}$ of the catalyst) on the GCE disk; and third, air-drying about 5 min at room temperature and then at 80 $^\circ\text{C}$ to yield a uniform thin film of the catalyst. The 0.5 M sulfuric acid was used as supporting electrolyte for all of the experiments. Besides, chronoamperometric analysis was applied to measure the stability of all catalysts in sulfuric acid and methanol.

3. RESULTS AND DISCUSSION

Structural Characterization of Ternary Fe_{1-x}PtRu_x NCs. Binary Fe₅₈Pt₄₂ NCs were synthesized by following a previous report with some modifications.¹² Three Fe_{1-x}PtRu_x ternary NCs, that is, Fe₃₅Pt₄₀Ru₂₅, Fe₃₁Pt₄₀Ru₂₉, and Fe₁₇Pt₄₀Ru₄₃, were prepared by the reaction of Fe₅₈Pt₄₂ NCs and RuCl₃ in an ethanolic solution for 3, 10, and 15 h, respectively (Figure 1). The compositions and structural properties of binary Fe₅₈Pt₄₂ and ternary Fe_{1-x}PtRu_x NCs were determined by HRTEM, XRD, XANES, and EXAFS as discussed below.

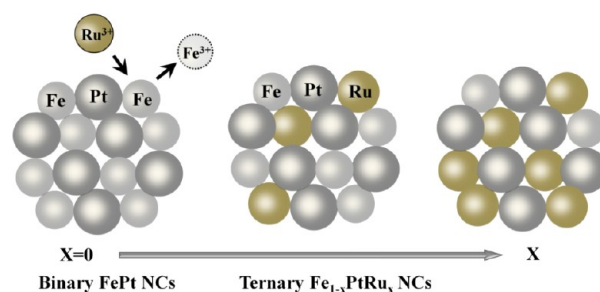


Figure 1. Schematic illustration of the cation replacement reaction from binary FePt to ternary Fe_{1-x}PtRu_x NCs in solution. During the reaction, Fe atoms of FePt NCs were gradually replaced by Ru atoms to form Fe_{1-x}PtRu_x NCs. By controlling the reaction time, the Ru content of Fe_{1-x}PtRu_x NCs was varied.

Figure 2 showed representative TEM images of well-dispersed binary Fe₅₈Pt₄₂ and ternary Fe_{1-x}PtRu_x NCs with

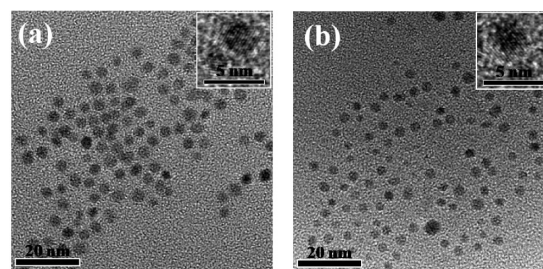


Figure 2. High-resolution TEM images of (a) binary Fe₅₈Pt₄₂ and (b) representative ternary Fe_{1-x}PtRu_x NCs. The averaged particle sizes are around $\sim 3\text{--}4 \text{ nm}$ for both samples. The lattice fringes of the samples were observed clearly in the images (insets of upper corner), showing that the crystal structures were well maintained after the cation replacement reaction.

particle sizes $\sim 3\text{--}4 \text{ nm}$. HRTEM images indicated that the NCs were crystalline with clear lattice structures. The d -spacing of all samples in Figure 2 was calculated to be $\sim 0.236 \text{ nm}$, which matches the (111) plane of face-centered cubic FePt.¹¹ The representative XRD patterns of binary Fe₅₈Pt₄₂ and ternary Fe_{1-x}PtRu_x NCs are presented in Figure 3. The main characteristic peaks of fcc crystalline Pt (JCPDS 04-802) were found at 2θ values of ca. 40° , 48° , 70° , and 84° , corresponding to the planes (111), (200), (220), and (311), respectively. The overall results indicated that all of the NCs were single crystal phase.

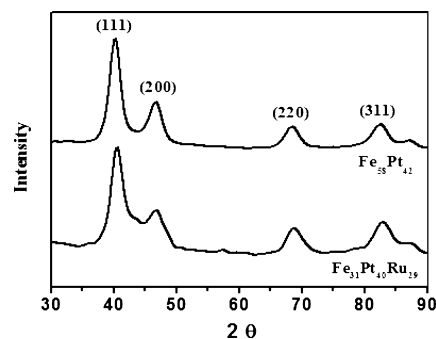


Figure 3. Powder XRD patterns of binary Fe₅₈Pt₄₂ NCs and representative ternary Fe_{1-x}PtRu_x NCs.

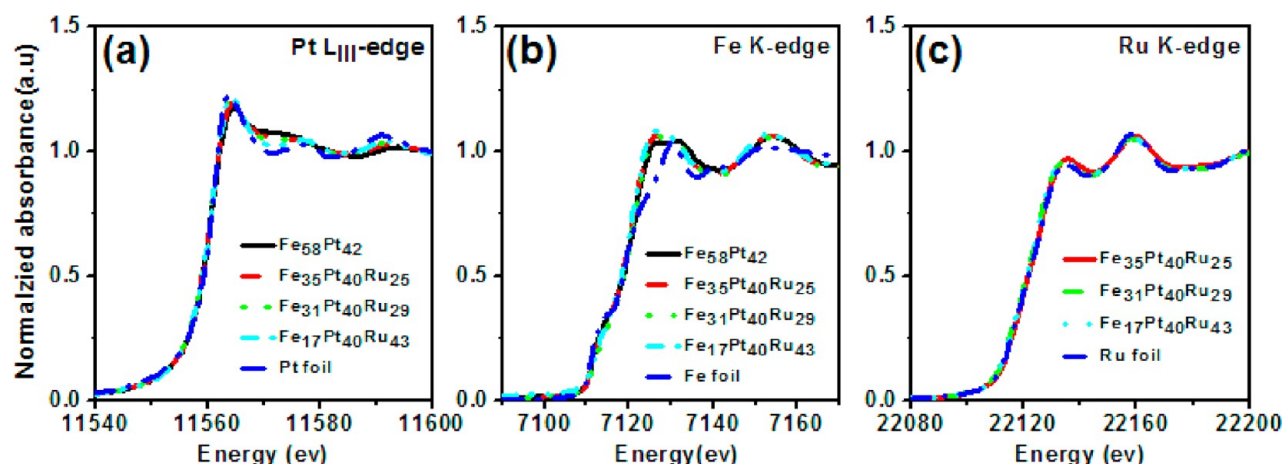


Figure 4. Normalized XANES spectra near the (a) Pt L_{III} -edge of binary $Fe_{58}Pt_{42}$ NCs and ternary $Fe_{1-x}PtRu_x$ and Fe foil; (b) Fe K-edge of binary $Fe_{58}Pt_{42}$ NCs and ternary $Fe_{1-x}PtRu_x$ and Pt foil; and (c) Ru K-edge of ternary $Fe_{1-x}PtRu_x$ NCs and Ru foil.

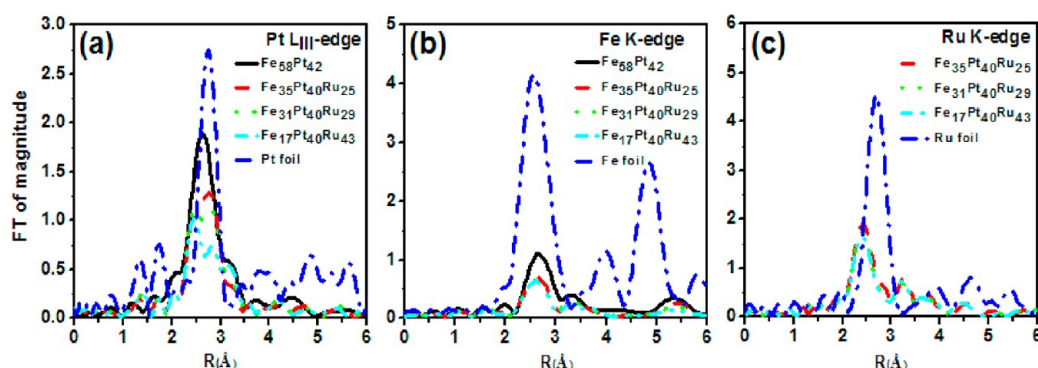


Figure 5. FT-EXAFS spectra at the (a) Pt L_{III} -edge of binary $Fe_{58}Pt_{42}$ NCs and ternary $Fe_{1-x}PtRu_x$ and Fe foil; (b) Fe K-edge of binary $Fe_{58}Pt_{42}$ NCs and ternary $Fe_{1-x}PtRu_x$ and Pt foil; and (c) Ru K-edge of ternary $Fe_{1-x}PtRu_x$ NCs and Ru foil.

Electronic Properties of the Local Environment of Binary $Fe_{58}Pt_{42}$ and Ternary $Fe_{1-x}PtRu_x$ NCs – Determined by XANES Analysis. To understand the details of the electronic state of the binary $Fe_{58}Pt_{42}$ and ternary $Fe_{1-x}PtRu_x$ NCs, XANES of Pt L_{III} -edge, Fe K-edge, and Ru K-edge was performed (Figure 4). The XANES spectra of Pt L_{III} -edges of the NCs and Pt foil are shown in Figure 4a. The absorption at 11 564 eV corresponds to the $2p_{3/2}$ –5d electronic transition of Pt metal. The magnitude of this absorption is termed the white line, small reductions of which were observed for the binary and ternary NCs as compared to the reference Pt foil. Variations in the Pt white line intensity were attributed to the alloying of Fe or Ru with Pt, leading to more electronic hybrids with Pt 5d electronic states. Figure 4b shows XANES patterns of the Fe K-edge of the binary $Fe_{58}Pt_{42}$ and ternary $Fe_{1-x}PtRu_x$ NCs and a Fe foil. The pre-edge feature of the reference Fe foil, originating from the 1s to 3d transition, was observed at 7709 eV; see Figure 4b. This feature is the fingerprint for the tetrahedral site symmetry of iron species in Fe foil. In contrast, this pre-edge feature disappeared completely from binary and ternary NCs, indicating that alloyed $Fe_{1-x}PtRu_x$ structure was formed only, but no iron oxide was found on the surface of ternary $Fe_{1-x}PtRu_x$ NCs after the annealing under H_2 at 300 °C. The absence of the pre-edge peak also indicates that a 1s to 3d transition in the octahedrally symmetrical Fe atom is forbidden. In Figure 4b, it is interesting to note that the absorption edges of all binary and ternary NCs move toward a slightly higher energy region when compared to those of the Fe foil. This may

be due to the heteroatomic interaction or nanosized effect in the binary and ternary NCs. In Figure 4c, the XANES feature of the Ru K-edge of the ternary $Fe_{1-x}PtRu_x$ NCs is close to that of the reference Ru foil, confirming that the oxidation state of Ru of the ternary NCs should be zero and not 3^+ , as was the case for the solvated Ru ions before the reaction.

Detailed Structural Properties of the Binary $Fe_{58}Pt_{42}$ and Ternary $Fe_{1-x}PtRu_x$ NCs – Determined by EXAFS Analysis. To understand the detailed structural properties of the binary $Fe_{58}Pt_{42}$ and ternary $Fe_{1-x}PtRu_x$ NCs, Fourier transformed (FT) k^3 -weighted EXAFS spectra were obtained; see Figure 5. Figure 5a shows that the FT peaks of the binary and ternary NCs at the Pt L_{III} -edge appeared shifted between 2 and 3 Å in comparison with that of reference Pt. The peak centered at ca. 2.5 Å in the NCs FT spectra results from contributions related to the first Pt–Fe, Pt–Pt, and Pt–Ru coordination shell. The peak splitting at the Pt L_{III} -edge corresponds to the interference between backscattering from neighboring Fe, Ru, and Pt. The splitting pattern suggests the formation of Pt–Fe and Pt–Ru clusters after the reaction. Figure 5b shows k^3 -weighted EXAFS spectra at the Fe K-edge of binary and ternary NCs. The broad peak between 2.0 and 3.3 Å of the spectra corresponded to the Fe–Fe, Fe–Pt, and Fe–Ru first shell coordination. The FT k^3 -weighted EXAFS spectra at the Ru K-edge (Figure 5c) also exhibited the peak in the R range of 2–3 Å, due to first shell metal–metal bonding involving Ru–Pt, Ru–Fe, and Ru–Ru correlations. The best fit EXAFS parameters including the coordination numbers (N)

Table 1. EXAFS Fitting Parameters at the Pt L_{III}-Edge, Fe K-Edge, and Ru K-Edge of Fe_{1-x}PtRu_x^a

samples	shell	N	R _i (Å)	σ ² × 10 ⁻³ (Å ²)	ΔE ₀ (eV)
Pt L _{III} -Edge					
Fe ₅₈ Pt ₄₂	Pt–Pt	2.7(±0.4)	2.718(±0.005)	4.1(±0.7)	8.56
	Pt–Fe	7.3(±0.4)	2.662(±0.002)	9.7(±0.3)	1.48
Fe ₃₅ Pt ₄₀ Ru ₂₅	Pt–Pt	2.7(±0.4)	2.719(±0.019)	5.7(±0.9)	9.63
	Pt–Fe	3.9(±0.2)	2.661(±0.008)	9.8(±1.4)	0.69
	Pt–Ru	0.7(±0.1)	2.684(±0.020)	12.1(±2.0)	9.59
Fe ₃₁ Pt ₄₀ Ru ₂₉	Pt–Pt	2.7(±1.2)	2.718(±0.017)	4.0(±0.9)	9.48
	Pt–Fe	3.9(±0.3)	2.660(±0.012)	1.8(±2.1)	−1.91
	Pt–Ru	0.8(±0.3)	2.684(±0.015)	0.0(±1.6)	9.24
Fe ₁₇ Pt ₄₀ Ru ₄₃	Pt–Pt	2.7(±0.4)	2.717(±0.027)	4.0(±0.4)	8.93
	Pt–Fe	2.8(±0.3)	2.660(±0.014)	6.5(±2.6)	−1.91
	Pt–Ru	0.9(±0.2)	2.682(±0.020)	0.8(±1.8)	6.22
Fe K-Edge					
Fe ₅₈ Pt ₄₂	Fe–Pt	5.3(±0.9)	2.662(±0.016)	11.0(±2.3)	2.15
	Fe–Fe	2.0(±0.4)	2.580(±0.020)	9.6(±3.0)	−10.20
Fe ₃₅ Pt ₄₀ Ru ₂₅	Fe–Pt	4.4(±0.7)	2.661(±0.018)	7.4(±3.4)	−1.14
	Fe–Ru	0.5(±0.3)	2.648(±0.052)	3.9(±1.6)	11.33
Fe ₃₁ Pt ₄₀ Ru ₂₉	Fe–Pt	4.8(±1.6)	2.660(±0.050)	0.1(±0.9)	0.09
	Fe–Ru	0.4(±0.1)	2.648(±0.010)	0.0(±2.0)	0.31
Fe ₁₇ Pt ₄₀ Ru ₄₃	Fe–Pt	6.9(±2.0)	2.660(±0.028)	14.8(±4.0)	0.09
Ru K-Edge					
Fe ₃₅ Pt ₄₀ Ru ₂₅	Ru–Pt	1.0(±0.8)	2.684(±0.052)	12.1(±6.1)	−7.12
	Ru–Ru	5.3(±0.3)	2.674(±0.006)	4.2(±0.7)	3.54
	Ru–Fe	0.7(±0.6)	2.648(±0.036)	2.0(±0.6)	2.79
Fe ₃₁ Pt ₄₀ Ru ₂₉	Ru–Pt	1.2(±0.6)	2.684(±0.040)	6.0(±4.9)	−6.43
	Ru–Ru	4.6(±0.2)	2.673(±0.007)	4.4(±0.6)	2.94
	Ru–Fe	0.4(±0.2)	2.648(±0.013)	2.0(±1.7)	6.04
Fe ₁₇ Pt ₄₀ Ru ₄₃	Ru–Pt	0.8(±0.7)	2.682(±0.020)	1.1(±2.0)	−2.33
	Ru–Ru	4.2(±0.3)	2.674(±0.004)	3.9(±0.5)	2.09

^aN, coordination number; R_i, bonding distance; σ², Debye–Waller factor; ΔE₀, inner potential shift.

Table 2. Coordination Numbers, Alloying Extent Values, and Surface Compositions for Pt, Fe, and Ru Calculated from XAS Experimental Results of Binary FePt/C NCs and Ternary Fe_{1-x}PtRu_x/C NCs

sample	ΣN _{Pt-i}	P _{obsd}	J _{Pt} (%)	ΣN _{Fe-i}	R _{obsd}	J _{Fe} (%)	ΣN _{Ru-i}	S _{obsd}	J _{Ru} (%)
Fe ₅₈ Pt ₄₂	10	0.7	126	7.3	0.7	174			
Fe ₃₅ Pt ₄₀ Ru ₂₅	7.3	0.6	104	4.9	1	154	7.1	0.2	33
Fe ₃₁ Pt ₄₀ Ru ₂₉	7.4	0.6	104	5.2	1	145	6.2	0.3	35
Fe ₁₇ Pt ₄₀ Ru ₄₃	6.4	0.6	96	6.9	1	120	5.1	0.2	29

and bond distances (R) of the binary and ternary NCs are shown below, and the detailed structural changes of the NCs during cation replacement reaction are discussed.

Table 1 lists the coordination numbers (N), bond distances (R), and the Debye–Waller factor (Δσ²) extracted from the EXAFS spectra of the binary Fe₅₈Pt₄₂ and ternary Fe_{1-x}PtRu_x NCs. The changes of the coordination numbers suggest that the atomic distribution of the binary and ternary NCs varied, while some Fe atoms of Fe₅₈Pt₄₂ NCs were replaced by Ru ions in the solution after the reaction. On the basis of the coordination numbers and bond distances in Table 1, the structural changes related to the structural transformation of binary Fe₅₈Pt₄₂NCs to ternary Fe_{1-x}PtRu_x NCs (Figure 1) can be understood. Here, the Pt atoms and Fe atoms of Fe₅₈Pt₄₂ NCs are preferentially located in the core region and in the shell region, respectively, because the total coordination number of metallic Fe atoms (N_{Fe–Pt} + N_{Fe–Fe}) of Fe₅₈Pt₄₂ NCs is less than that of metallic Pt atoms (N_{Pt–Fe} + N_{Pt–Pt}). We found that the Pt atoms of Fe₅₈Pt₄₂ NCs were not dissolved from the NCs into the solution when the cation replacement

reaction was proceeding. However, we confirmed that the Fe atoms of Fe₅₈Pt₄₂ NCs dissolved gradually after the addition of RuCl₃, based on the decrease of the coordination number of N_{Pt–Fe}. From the coordination numbers of N_{Ru–Pt}, N_{Ru–Ru}, and N_{Ru–Fe} in the three ternary Fe_{1-x}PtRu_x NCs, we can suggest that more Ru atoms are reduced on the Fe₅₈Pt₄₂ NCs with an increase in the cation replacement reaction time. In Table 1, N_{Ru–Ru} coordination is much larger than N_{Ru–Fe} and N_{Ru–Pt}. The reason could be corresponded to that, during the replacement reaction between Fe and Ru on the NC surface, a Ru-rich shell may form. Overall, the results show that the atomic distribution of Fe₃₅Pt₄₀Ru₂₅, Fe₃₁Pt₄₀Ru₂₉, and Fe₁₇Pt₄₀Ru₄₃ NCs can be deduced from these changes of coordination numbers of the binary and ternary NCs.

Alloying Extent (J_{Pt}, J_{Fe}, and J_{Ru}) of the Binary Fe₅₈Pt₄₂ and Ternary Fe_{1-x}PtRu_x NCs. Previous studies have suggested that the catalytic activity of metal alloyed NCs shows a strong dependency on the alloying extent. XAS analysis was applied to determine the alloying extent and atomic distribution of the binary Fe₅₈Pt₄₂ NCs and ternary Fe_{1-x}PtRu_x

NCs with different cation replacement reaction times. The alloying extents of $\text{Fe}_{1-x}\text{PtRu}_x$ NCs were calculated on the basis of the structural parameters obtained from XAS measurements (see the Supporting Information). The J_{Pt} , J_{Fe} , and J_{Ru} of the binary $\text{Fe}_{58}\text{Pt}_{42}$ and ternary $\text{Fe}_{1-x}\text{PtRu}_x$ NCs are shown in Table 2. The values of J_{Pt} (126%) and J_{Fe} (174%) of $\text{Fe}_{58}\text{Pt}_{42}$ NCs indicated that most of the Pt and Fe in the $\text{Fe}_{58}\text{Pt}_{42}$ NCs existed in the alloyed state. Although the three ternary $\text{Fe}_{1-x}\text{PtRu}_x$ NCs underwent the cation replacement process, the J_{Pt} and J_{Fe} of the ternary $\text{Fe}_{1-x}\text{PtRu}_x$ NCs were still larger than 100%. The J_{Pt} and J_{Fe} (larger than 100%) of the ternary $\text{Fe}_{1-x}\text{PtRu}_x$ NCs indicate that the Pt and Fe atoms in the NCs retained a high alloying extent during the cation replacement reaction. However, the result of low J_{Ru} of the ternary $\text{Fe}_{1-x}\text{PtRu}_x$ NCs indicated that some segregation of Ru atoms in the NCs occurred.³⁵ According to the alloying extent data of the ternary $\text{Fe}_{1-x}\text{PtRu}_x$ NCs, different electrochemical catalytic activities are expected (see below).

Electrocatalytic Properties of the Binary $\text{Fe}_{58}\text{Pt}_{42}$ and Ternary $\text{Fe}_{1-x}\text{PtRu}_x$ NCs in the Methanol Oxidation Reaction. To examine the catalytic activities of the binary $\text{Fe}_{58}\text{Pt}_{42}$ NCs and ternary $\text{Fe}_{1-x}\text{PtRu}_x$ NCs in the MOR, linear sweep voltammograms (LSV) of the binary $\text{Fe}_{58}\text{Pt}_{42}$, J-M PtRu, and three ternary $\text{Fe}_{1-x}\text{PtRu}_x$ NCs were performed in methanol solution. In Figure 6, the potential peak at ca. 0.7 V of all of the

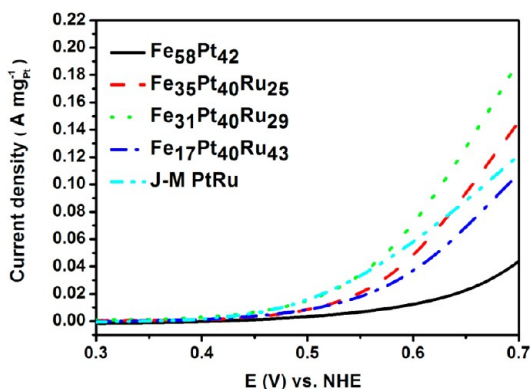


Figure 6. Linear sweep voltammograms (LSV) of binary $\text{Fe}_{58}\text{Pt}_{42}$ NCs, ternary $\text{Fe}_{1-x}\text{PtRu}_x$, and J-M PtRu catalysts (in 0.5 M H_2SO_4 with 10 vol % CH_3OH at 25 °C, scan rate = 10 mV/s).

samples during the forward scan is normally attributed to catalytic activity during the MOR. We found that the anodic current density of ternary $\text{Fe}_{31}\text{Pt}_{40}\text{Ru}_{29}$ NCs was 1.5-fold that of J-M PtRu NCs at 0.7 V. Besides the differences in the anodic current density, the onset potential for $\text{Fe}_{58}\text{Pt}_{42}$ NCs was measured at 0.50 V. On introducing Ru, the onset potential decreased from 0.50 V ($\text{Fe}_{58}\text{Pt}_{42}$ NCs) to 0.48 V ($\text{Fe}_{35}\text{Pt}_{40}\text{Ru}_{25}$ NCs) and 0.45 V ($\text{Fe}_{31}\text{Pt}_{40}\text{Ru}_{29}$ NCs), respectively, with the increase of alloying extent of Ru. Among the binary $\text{Fe}_{58}\text{Pt}_{42}$ NCs and ternary $\text{Fe}_{1-x}\text{PtRu}_x$ NCs, $\text{Fe}_{31}\text{Pt}_{40}\text{Ru}_{29}$ NCs with the highest J_{Ru} were found to have the lowest onset potential (~ 0.45 V), that is, similar to that of J-M PtRu NCs. The onset potential (near 0.4–0.5 V) represents the effectiveness in removing the incompletely oxidized carbonaceous species formed during the oxidation reaction. On the basis of our results for the onset potential and anodic current density in Figure 6, the catalytic activity showed a dependency on the alloying extent of Ru atom in the ternary $\text{Fe}_{1-x}\text{PtRu}_x$ NCs (see Table 2). Also, our measurements showed that the ternary

$\text{Fe}_{31}\text{Pt}_{40}\text{Ru}_{29}$ NCs exhibited the best catalytic activity among all five samples including J-M PtRu NCs.

A simple model is proposed to understand the differences in the catalytic activity between the binary $\text{Fe}_{58}\text{Pt}_{42}$ and ternary $\text{Fe}_{1-x}\text{PtRu}_x$ NCs. With the presence of Ru in ternary $\text{Fe}_{1-x}\text{PtRu}_x$ NCs, the formation of Ru–OH on the surface of the NCs is expected, thus allowing the adsorbed water molecule to be discharged by the Ru–OH species at a less positive potential, thereby causing a lower onset potential.³³ The electron charge transfer from Fe and Ru to Pt can assist in oxidizing the poisoning intermediate, that is, CO, on the Pt site to form CO_2 , resulting in an improvement in the current density for the MOR. The details of the charge transfer in the ternary NCs were studied by theoretical calculation, as described below to understand the origin of the catalytic activity enhancement.

Anti-CO Poisoning Measurements of the Binary $\text{Fe}_{58}\text{Pt}_{42}$ and Ternary $\text{Fe}_{1-x}\text{PtRu}_x$ NCs. To study the catalytic activity of CO monolayer oxidation on the binary $\text{Fe}_{58}\text{Pt}_{42}$, J-M PtRu, and the three ternary $\text{Fe}_{1-x}\text{PtRu}_x$ NCs, the CO stripping voltammograms were measured. As is shown in Figure 7, the

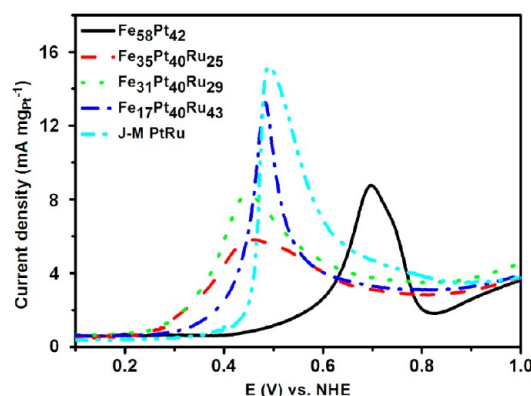


Figure 7. CO-stripping voltammograms of binary $\text{Fe}_{58}\text{Pt}_{42}$ NCs, ternary $\text{Fe}_{1-x}\text{PtRu}_x$, and J-M PtRu catalysts in 0.5 M H_2SO_4 at 25 °C (scanning rate: 20 mV/s).

onset potentials of ternary $\text{Fe}_{1-x}\text{PtRu}_x$ NCs samples were clearly lower than those of binary J-M PtRu NCs and $\text{Fe}_{58}\text{Pt}_{42}$ NCs. Also, $\text{Fe}_{31}\text{Pt}_{40}\text{Ru}_{29}$ NCs exhibited the lowest onset potential (0.244 V) among the ternary $\text{Fe}_{1-x}\text{PtRu}_x$ NCs. The results suggested that the ternary $\text{Fe}_{1-x}\text{PtRu}_x$ NCs exhibited a superior ability to resist CO poisoning on the NC's surface in comparison to binary $\text{Fe}_{58}\text{Pt}_{42}$ NCs and the J-M PtRu. Also, ternary $\text{Fe}_{1-x}\text{PtRu}_x$ NCs reduce the polarization overpotential in the activation of MOR, thereby giving a higher catalytic current density. Previous theoretical studies have shown that alloying Pt with Ru leads to effectively modifying the electronic structure of Pt by the surrounding Ru atom, resulting in a lowering of CO adsorption energy on Pt.^{24,40} In our work, with proper adjustment of the Fe, Pt, and Ru ratios of the ternary $\text{Fe}_{1-x}\text{PtRu}_x$ NCs, the catalytic activity for CO monolayer oxidation can be easily enhanced by a simple cation replacement reaction in the solution. The enhanced catalytic activity for CO monolayer oxidation in the ternary $\text{Fe}_x\text{PtRu}_{1-x}$ NCs could also be attributed to the electron charge transfer from Fe and Ru to Pt, resulting in a change in the adsorption energy of the CO molecule adsorbed on the surface of the ternary $\text{Fe}_x\text{PtRu}_{1-x}$ NCs.

Stability Measurements of the Binary $\text{Fe}_{58}\text{Pt}_{42}$ and Ternary $\text{Fe}_{1-x}\text{PtRu}_x$ NCs. The chronoamperometric analyses were applied to test the stability of metal alloyed NCs (Figure 8). The chronoamperometric curves indicated that $\text{Fe}_{31}\text{Pt}_{40}\text{Ru}_{29}$

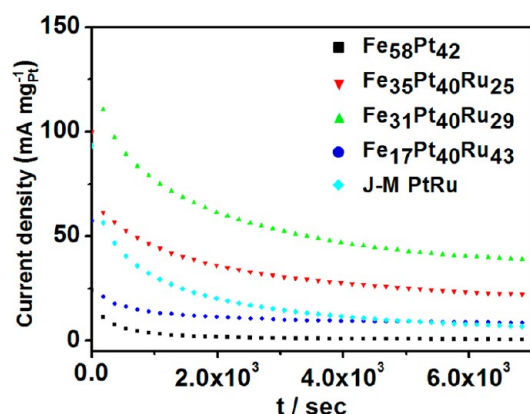


Figure 8. Chronoamperometric curves for binary $\text{Fe}_{58}\text{Pt}_{42}$ NCs, ternary $\text{Fe}_{1-x}\text{PtRu}_x$ and J-M PtRu catalysts in 0.5 M sulfuric acid with 10 vol % methanol. The measurements were performed at a fixed voltage of 0.7 V in 0.5 M sulfuric acid with 10 vol % methanol for 7000 s.

and $\text{Fe}_{35}\text{Pt}_{40}\text{Ru}_{25}$ NCs possessed higher initial and limit potentiostatic current than J-M PtRu over the period of 2 h. Without replacement by Ru, $\text{Fe}_{58}\text{Pt}_{42}$ NCs showed the lowest current among all of the catalysts. The results also indicated that the ternary $\text{Fe}_{31}\text{Pt}_{40}\text{Ru}_{29}$ NCs demonstrated the highest catalytic activity for eliminating the formation of intermediate species and best stability for oxidizing methanol molecules among the binary $\text{Fe}_{58}\text{Pt}_{42}$ NCs, J-M PtRu NCs, and ternary $\text{Fe}_{1-x}\text{PtRu}_x$ NCs. However, in the initial period of time, the potentiostatic current decreases rapidly for all of the NCs. The decreases were attributed to the formation intermediate species, such as adsorption of CO, CH_3OH , and CHO, during the methanol oxidation reaction.²³ Also, the dissolution of the Ru and Fe atoms of NCs in an acidic condition might cause the decrease of the current density.^{16,41}

Theoretical Modeling of CO Adsorption Energy and Transfer Charge on the Surface of the Binary and Ternary NCs. A theoretical simulation was performed to establish a model for understanding the atomic interaction of absorbed CO on the surface of bare Pt, binary $\text{Fe}_{58}\text{Pt}_{42}$, $\text{Pt}_{14}\text{Ru}_{13}$, and ternary $\text{Fe}_{31}\text{Pt}_{40}\text{Ru}_{29}$ NCs. Here, the adsorption energy (E_{ads}) of CO on the NCs' surfaces and the amount of charge transfer^{47,48} from the transition metal to the Pt atom were calculated. The results are presented in Table 3. The DFT computation procedures can be briefly described as follows. Simplified simulations were undertaken using bare Pt(111), $\text{Fe}_{58}\text{Pt}_{42}(111)$, $\text{Pt}_{14}\text{Ru}_{13}(111)$, and $\text{Fe}_{31}\text{Pt}_{40}\text{Ru}_{29}(111)$ slabs to model the E_{ads} of CO on those slabs (see the Supporting Information). The adsorbate molecule was considered to adsorb and attach on those slabs. The E_{ads} of CO was computed using DFT simulations of the slabs with one carbon monoxide molecule. The capping effect of CO was derived in terms of the adsorption energy (E_{ads}) of CO on the slabs and the residual surface charge on the CO and the slabs, with the help of ab initio simulations. The adsorption energy, E_{ads} , is defined as the sum of interactions between the adsorbate molecule and slab atoms, and it is given as $E_{\text{ads}} = E_{\text{total}} - E_{\text{slab}} - E_{\text{CO}}$, where E_{total} , E_{slab} , and E_{CO} are the total energy of the

Table 3. CO Adsorption Energy and Bader Charge Analysis in Pt(111), Fe(100), Ru(0001), $\text{Pt}_{58}\text{Fe}_{42}(111)$, $\text{Pt}_{14}\text{Ru}_{13}(111)$, and $\text{Fe}_{31}\text{Pt}_{40}\text{Ru}_{29}(111)$ Systems

species	CO E_{ads} (eV)	charge (e)	charge difference (e)
Pt(111)	−1.65	Pt: 10.041	
Fe(100)		Fe: 7.916	
Ru(0001)		Ru: 8.046	
$\text{Fe}_{58}\text{Pt}_{42}(111)$	−1.53	Pt: 10.484	Pt: 10.041 − 10.484 = −0.443
		Fe: 7.546	Fe: 7.916 − 7.546 = +0.370
$\text{Pt}_{14}\text{Ru}_{13}(111)$	−1.46	Pt: 10.300	Pt: 10.041 − 10.300 = −0.259
		Ru: 7.738	Ru: 8.046 − 7.738 = +0.308
$\text{Fe}_{31}\text{Pt}_{40}\text{Ru}_{29}(111)$	−1.3	Pt: 10.628	Pt: 10.041 − 10.628 = −0.587
		Ru: 7.623	Ru: 8.046 − 7.623 = +0.423
		Fe: 7.405	Fe: 7.916 − 7.405 = +0.557

system, slab energy, and adsorbate molecule energy, respectively. We have verified that the main contribution to the adsorption energy arose from the interactions of the slabs with the CO molecule via the charges on the slabs and CO. To confirm the feasibility of our established model using DFT simulation, the CO adsorption energy of Pt(111) was calculated first. The results showed a good agreement with the data in the previous reports; for example, the E_{ads} of CO on Pt(111) was obtained as being ca. −1.65 to −1.70 eV by DFT calculations.^{49,50} After the CO adsorption energy calculation, Bader charge analyses were carried out for bare Pt(111)–CO, $\text{Fe}_{58}\text{Pt}_{42}(111)$ –CO, $\text{Pt}_{14}\text{Ru}_{13}(111)$ –CO, and $\text{Fe}_{31}\text{Pt}_{40}\text{Ru}_{29}(111)$ –CO to calculate the electron charge transfer from transition metal atom to Pt atom in binary and ternary alloy NCs.

The C–O adsorption energies on the surfaces of Pt(111), $\text{Fe}_{58}\text{Pt}_{42}(111)$, $\text{Pt}_{14}\text{Ru}_{13}(111)$, and $\text{Fe}_{31}\text{Pt}_{40}\text{Ru}_{29}(111)$ are shown in Table 3. In $\text{Fe}_{58}\text{Pt}_{42}(111)$ –CO and $\text{Pt}_{14}\text{Ru}_{13}(111)$ –CO systems, CO adsorption on Pt was significantly affected due to specific interactions of Ru and Fe. The adsorption energy of CO_{ads} decreased considerably to −1.53 eV in the $\text{Fe}_{58}\text{Pt}_{42}(111)$ –CO slab, as compared to −1.65 eV for CO_{ads} on the Pt(111) surface. Considering the ternary $\text{Fe}_{31}\text{Pt}_{40}\text{Ru}_{29}(111)$ –CO system, upon CO adsorption, the Ru and Fe of the $\text{Fe}_{31}\text{Pt}_{40}\text{Ru}_{29}$ system thus lower the CO adsorption energy and weaken the C–O bond, as reflected in the considerable adsorption energy decrease of CO_{ads} to −1.30 eV.

Besides the adsorption energy, the calculation results of charge transfer in Pt, binary, and ternary NCs are also listed in Table 3. The simulation results clearly showed that charge transfer occurs from the transition metal to Pt in the binary and ternary NCs. This charge transfer has been considered as an important factor that can influence the adsorption energy of gaseous molecule (i.e., CO) adsorbed on the catalysts' surfaces.⁴⁹ This information strongly supports the idea that the 5d-electron density around the Pt atoms in the binary and ternary alloys was increased due to partial electron transfer from the transition metal atoms to Pt atoms. This partial electronic transfer effect was carried out from first-principles in the DFT modeling study. The result of charge transfer was used to explain the variations in E_{ads} in the binary and ternary NCs. The results showed that in the $\text{Fe}_{58}\text{Pt}_{42}(111)$ and $\text{Pt}_{14}\text{Ru}_{13}(111)$ systems, the charge on platinum was increased

from 10.041 e (for the bare Pt) to 10.484 and 10.300 e, respectively. The increases in charge transfer are quite reasonable, because charge transfer from Ru or Fe atom to Pt can easily occur in $\text{Fe}_{58}\text{Pt}_{42}(111)$ and $\text{Pt}_{14}\text{Ru}_{13}(111)$ systems. On the other hand, in the $\text{Fe}_{31}\text{Pt}_{40}\text{Ru}_{29}(111)$ system, the charge on the platinum atom was increased to 10.628 e. The increases of charge transfer in the $\text{Fe}_{31}\text{Pt}_{40}\text{Ru}_{29}(111)$ system in comparison with $\text{Pt}(111)$ are larger than those in the $\text{Fe}_{58}\text{Pt}_{42}(111)$ and $\text{Pt}_{14}\text{Ru}_{13}(111)$ systems. The results showing charge transfer for binary and ternary NCs in Table 3 offer convincing evidence that the second elements of Ru and Fe can lead to much lower adsorption energies for the adsorption of CO on $\text{Fe}_{58}\text{Pt}_{42}(111)$, $\text{Pt}_{14}\text{Ru}_{13}(111)$, and $\text{Fe}_{31}\text{Pt}_{40}\text{Ru}_{29}(111)$ surfaces.

Electron Density Contour of CO Adsorption Energy.

To specify the different strengths of CO bonding between Pt atom and CO molecules in pure Pt, binary, and ternary NCs, the electron density contour maps of $\text{Pt}(111)\text{-CO}$, $\text{Pt}_{58}\text{Fe}_{42}(111)\text{-CO}$, $\text{Pt}_{14}\text{Ru}_{13}(111)\text{-CO}$, and $\text{Fe}_{31}\text{Pt}_{40}\text{Ru}_{29}(111)\text{-CO}$ in Figure 9 were obtained. Here, the DFT calculation was performed on the basis of the structural models described in the Supporting Information. The electron density contours of the planes were cut through the center site of the Pt atoms and the transition metal atoms. Figure 9a shows that the bonding between CO and the Pt surface is due to the coupling of the CO 5σ orbital to the surface and the back-donating of electrons from the substrate to the $2\pi^*$ orbital of the CO molecule. Figure 9b–d shows that CO adsorption on Pt sites, on the ternary $\text{Fe}_{31}\text{Pt}_{40}\text{Ru}_{29}$ surfaces, is considerably weaker than that on bare Pt and binary $\text{Pt}_{58}\text{Ru}_{42}$ and $\text{Pt}_{14}\text{Ru}_{13}$. It was well-known that an unoccupied d-orbital on a Pt surface tends to obtain electrons from CO molecules.^{49,50} Therefore, a very clear charge transfer from Ru or Fe to Pt and back-donating of electrons from the Pt to the orbital of CO molecule was found. Here, back-donation is an important factor that influences the adsorption energy of CO being adsorbed on the surface of the binary and ternary NCs. Obviously, the electron density between the C atom of the CO molecule and the bonded Pt of the ternary $\text{Fe}_{31}\text{Pt}_{40}\text{Ru}_{29}(111)$ surface is smaller than that in the binary $\text{Pt}_{58}\text{Ru}_{42}$ and $\text{Pt}_{14}\text{Ru}_{13}$ systems. The trend of electron density of Pt–CO bonding in the four cases is in the order: $\text{Pt}(111) > \text{Pt}_{58}\text{Ru}_{42}(111) > \text{Pt}_{14}\text{Ru}_{13}(111) > \text{Fe}_{31}\text{Pt}_{40}\text{Ru}_{29}(111)$. This trend also means that the strength of CO bonding in the four cases is: $\text{Pt}(111) > \text{Pt}_{58}\text{Ru}_{42}(111) > \text{Pt}_{14}\text{Ru}_{13}(111) > \text{Fe}_{31}\text{Pt}_{40}\text{Ru}_{29}(111)$. The calculation results here suggested that the charge transfer may be considered as one of the very important effects to alternate the adsorption energy of CO adsorbed on the catalytic surfaces.

Previous studies have indicated that 3d transition metals of catalytic NCs are able to release from the NC's surface in an acidic solution during the MOR.⁵¹ To consider the possible dissolution of Fe atoms from the surface of $\text{Fe}_{1-x}\text{PtRu}_x$ NCs, the DFT calculation was also executed on the basis of the structural model (see Figures S3 and S4) so that no Fe atom was located on the surface layer of the NCs. Figure 9e and f showed the electron density contour maps of $\text{Fe}_{58}\text{Pt}_{42}(111)\text{-CO}$ and $\text{Fe}_{31}\text{Pt}_{40}\text{Ru}_{29}(111)\text{-CO}$, respectively. The adsorption energy of $\text{Fe}_{58}\text{Pt}_{42}(111)\text{-CO}$ and $\text{Fe}_{31}\text{Pt}_{40}\text{Ru}_{29}(111)\text{-CO}$ was also calculated to be -1.53 and -1.31 eV, respectively. In comparison to the results in Figure 9b and d, only slight differences on both the electron density and the adsorption energy were obtained when the calculation was performed on the basis of two different structural models (with/without Fe

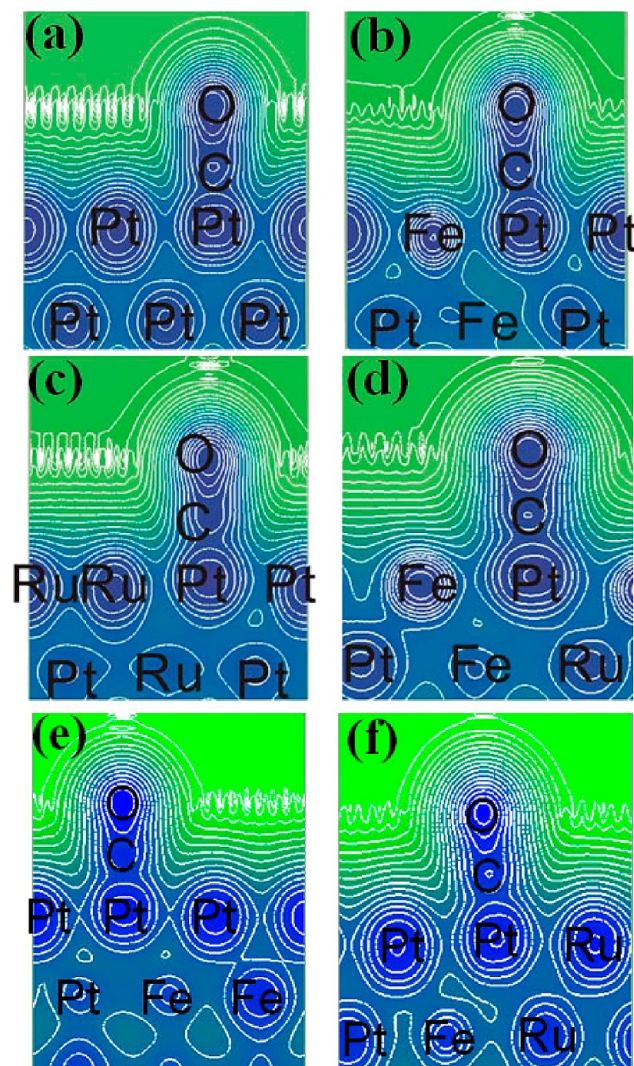


Figure 9. The electron density contour of the CO adsorbed on (a) bare Pt (111), binary (b) $\text{Fe}_{58}\text{Pt}_{42}$ (111), (c) $\text{Pt}_{14}\text{Ru}_{13}$ (111), (d) ternary $\text{Fe}_{31}\text{Pt}_{40}\text{Ru}_{29}$ (111) NCs surface, (e) $\text{Fe}_{58}\text{Pt}_{42}$ (111) without Fe atom on the NC's surface, and (f) $\text{Fe}_{31}\text{Pt}_{40}\text{Ru}_{29}$ (111) NCs without Fe atom on the NC's surface.

atoms on the surface of NCs). Thus, even if Fe atoms on the NC's surface were dissolved at the initial period of the reaction in the acid solution, the CO adsorption energy of ternary $\text{Fe}_{31}\text{Pt}_{40}\text{Ru}_{29}$ NCs was still much lower than that of binary NCs.

Charge Transfer Model for Catalytic Activity Enhancements. Our experimental results indicated that the catalytic activity of ternary $\text{Fe}_{1-x}\text{PtRu}_x$ NCs showed a strong dependency on the NC's alloying extent. Also, when the alloying extent of the NCs was increased, the catalytic activity for MOR was enhanced. To understand the origin of the enhancement of catalytic activity, a simple model was proposed on the basis of our simulation data. With the addition of Ru metal in $\text{Fe}_{58}\text{Pt}_{42}$ NCs, our calculation showed that the electronic structure of Pt was modified by electron charge transfer from Fe and Ru atoms to Pt atom in our resulting ternary $\text{Fe}_{1-x}\text{PtRu}_x$ NCs system. The strong charge transfer was found to cause the change in the Pt–CO absorption energy resulting in differences of catalytic activities in monoalloy, binary, and ternary systems (Figure 10). As compared to Pt and binary systems, ternary $\text{Fe}_{1-x}\text{PtRu}_x$ NCs ($x \neq 0$) systems showed that the adsorption energy of CO was

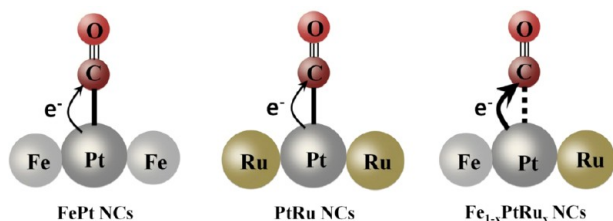


Figure 10. Schematic illustration of the CO adsorbed on the binary FePt, PtRu, and ternary $\text{Fe}_{1-x}\text{Pt}_x$ NCs. The arrows here represented the strength of electron charge transfer from Pt atom to CO molecule. The bonding (dashed line) of Pt–CO in the ternary $\text{Fe}_{1-x}\text{Pt}_x$ NCs is weaker than that (solid line) of Pt–CO of the binary FePt and PtRu NCs. Notice that the structural model represents here that Fe and Ru atoms could be located either on the surface or in the second layer of NCs.

lowered. The increase of electron charge transfer from the transition metal to Pt atom leads to the increase of electron back-donation from the 5d orbital of Pt atom to the unoccupied $2\pi^*$ orbital of the CO molecule. Several reports have indicated that the increase was the major factor for the weakening of CO–Pt bonding.^{52–55} The present work, supported with experiments and rationalized with accurate theoretical considerations, clearly demonstrates the unprecedented catalytic effect exerted by the ternary metal for the MOR.

The catalytic activity enhancement of the ternary $\text{Fe}_{1-x}\text{Pt}_x$ NCs, in comparison to the binary PtRu NCs, has been also observed in other nanocrystals, for example, with PtRuNi and PtRuIr. Previous proposed models have indicated that the enhancements were mainly attributed to two factors: (1) the ligand effect, whereby the electronic properties of Pt are modified by the orbital overlap of addition metal,³ and (2) the bifunctional effect, where addition metal facilitates the generation of oxygen-containing species on sites adjacent to Pt, thereby aiding in the oxidation of CO.⁵⁶ Therefore, the adjustment of the catalyst's structure to accord with the optimal electronic structure of Pt is the key to enhancing electrocatalytic activity in the MOR.

4. CONCLUSION

Ternary $\text{Fe}_{1-x}\text{Pt}_x$ NCs with different alloying extents have been successfully prepared using a simple solution reaction and have demonstrated significant catalytic utility when applied to the MOR. In comparison with the binary FePt and RuPt NCs, the superior CO poisoning resistance of the ternary $\text{Fe}_{1-x}\text{Pt}_x$ NCs was attributed to the weak bonding of CO to the Pt atom on the NC's surface based on the density functional theoretical simulation. Our studies have demonstrated a new and simple direction for the discovery of high-performance metal alloyed catalyst by adding cheap transition metal into binary PtRu NCs for fuel cell applications.

■ ASSOCIATED CONTENT

Supporting Information

DFT and alloying extent calculation. This material is available free of charge via the Internet at <http://pubs.acs.org>.

■ AUTHOR INFORMATION

Corresponding Author

cjchen@ntnu.edu.tw; bjh@mail.ntust.edu.tw

Notes

The authors declare no competing financial interest.

■ ACKNOWLEDGMENTS

This work is supported by the National Science Council, Taiwan (Project Nos. NSC 99-2120-M-003-001- and NSC 99-2811-M-011-005). We thank Dr. Rick John for editing this paper and the National Center for High-Performance Computing (NCHC) for providing computer facilities.

■ REFERENCES

- (1) Borup, R.; Meyers, J.; Pivovar, B.; Kim, Y. S.; Mukundan, R.; Garland, N.; Myers, D.; Wilson, M.; Garzon, F.; Wood, D.; Zelenay, P.; More, K.; Stroh, K.; Zawodzinski, T.; Boncella, J.; McGrath, J. E.; Inaba, M.; Miyatake, K.; Hori, M.; Ota, K.; Ogumi, Z.; Miyata, S.; Nishikata, A.; Siroma, Z.; Uchimoto, Y.; Yasuda, K.; Kimijima, K. I.; Iwashita, N. *Chem. Rev.* **2007**, *107*, 3904–3951.
- (2) Liu, H. S.; Song, C. J.; Zhang, L.; Zhang, J. J.; Wang, H. J.; Wilkinson, D. P. *J. Power Sources* **2006**, *155*, 95–110.
- (3) Wee, J. H.; Lee, K. Y. *J. Power Sources* **2006**, *157*, 128–135.
- (4) Bock, C.; Paquet, C.; Couillard, M.; Botton, G. A.; MacDougall, B. R. *J. Am. Chem. Soc.* **2004**, *126*, 8028.
- (5) Sau, T. K.; Lopez, M.; Goia, D. V. *Chem. Mater.* **2009**, *21*, 3649–3654.
- (6) Roth, C.; Benker, N.; Buhrmester, T.; Mazurek, M.; Loster, M.; Fuess, H.; Koningsberger, D. C.; Ramaker, D. E. *J. Am. Chem. Soc.* **2005**, *127*, 14607–14615.
- (7) Wu, G.; Li, L.; Xu, B. Q. *Electrochim. Acta* **2004**, *50*, 1–10.
- (8) Gavrilov, A. N.; Savinova, E. R.; Simonov, P. A.; Zaikovskii, V. I.; Cherepanova, S. V.; Tsirlina, G. A.; Parmon, V. N. *Phys. Chem. Chem. Phys.* **2007**, *9*, 5476–5489.
- (9) Stoupin, S.; Rivera, H.; Li, Z. R.; Segre, C. U.; Korzeniewski, C.; Casadonte, D. J.; Inoue, H.; Smotkin, E. S. *Phys. Chem. Chem. Phys.* **2008**, *10*, 6430–6437.
- (10) Wiltshire, R. J. K.; King, C. R.; Rose, A.; Wells, P. P.; Davies, H.; Hogarth, M. P.; Thompson, D.; Theobald, B.; Mosselmans, F. W.; Roberts, M.; Russell, A. E. *Phys. Chem. Chem. Phys.* **2009**, *11*, 2305–2313.
- (11) Sun, S. H.; Murray, C. B.; Weller, D.; Folks, L.; Moser, A. *Science* **2000**, *287*, 1989.
- (12) Wang, D. Y.; Chen, C. H.; Yen, H. C.; Lin, Y. L.; Huang, P. Y.; Hwang, B. J.; Chen, C. C. *J. Am. Chem. Soc.* **2007**, *129*, 1538.
- (13) Ley, K. L.; Liu, R. X.; Pu, C.; Fan, Q. B.; Leyarova, N.; Segre, C.; Smotkin, E. S. *J. Electrochem. Soc.* **1997**, *144*, 1543–1548.
- (14) Park, K. W.; Choi, J. H.; Ahn, K. S.; Sung, Y. E. *J. Phys. Chem. B* **2004**, *108*, 5989–5994.
- (15) Wang, Z. B.; Yin, G. P.; Lin, Y. G. *J. Power Sources* **2007**, *170*, 242–250.
- (16) Liang, Y. M.; Zhang, H. M.; Tian, Z. Q.; Zhu, X. B.; Wang, X. L.; Yi, B. L. *J. Phys. Chem. B* **2006**, *110*, 7828–7834.
- (17) Yang, L. X.; Allen, R. G.; Scott, K.; Christenson, P.; Roy, S. J. *Power Sources* **2004**, *137*, 257–263.
- (18) Huang, T.; Jiang, R. R.; Liu, J. L.; Zhuang, J. H.; Cai, W. B.; Yu, A. S. *Electrochim. Acta* **2009**, *54*, 4436–4440.
- (19) Kawaguchi, T.; Rachi, Y.; Sugimoto, W.; Murakami, Y.; Takasu, Y. *J. Appl. Electrochem.* **2006**, *36*, 1117–1125.
- (20) Eguiluz, K. I. B.; Salazar-Banda, G. R.; Miwa, D.; Machado, S. A. S.; Avaca, L. A. *J. Power Sources* **2008**, *179*, 42–49.
- (21) Geng, D. S.; Matsuki, D.; Wang, J. J.; Kawaguchi, T.; Sugimoto, W.; Takasu, Y. *J. Electrochem. Soc.* **2009**, *156*, B397–B402.
- (22) Liao, S. J.; Holmes, K. A.; Tsapraillis, H.; Birss, V. I. *J. Am. Chem. Soc.* **2006**, *128*, 3504–3505.
- (23) Zhu, J.; Cheng, F. Y.; Tao, Z. L.; Chen, J. J. *Phys. Chem. C* **2008**, *112*, 6337–6345.
- (24) Alayoglu, S.; Zavalij, P.; Eichhorn, B.; Wang, Q.; Frenkel, A. I.; Chupas, P. *ACS Nano* **2009**, *3*, 3127–3137.
- (25) Godoi, D. R. M.; Perez, J.; Villullas, H. M. *J. Phys. Chem. C* **2009**, *113*, 8518–8525.
- (26) Greeley, J.; Mavrikakis, M. *Nat. Mater.* **2004**, *3*, 810–815.
- (27) Wang, D.; Zhuang, L.; Lu, J. T. *J. Phys. Chem. C* **2007**, *111*, 16416–16422.

- (28) Russell, A. E.; Rose, A. *Chem. Rev.* **2004**, *104*, 4613–4635.
- (29) Bock, C.; Blakely, M. A.; MacDougall, B. *Electrochim. Acta* **2005**, *50*, 2401–2414.
- (30) Mpourmpakis, G.; Andriotis, A. N.; Vlachos, D. G. *Nano Lett.* **2010**, *10*, 1041–1045.
- (31) Pitois, A.; Davies, J. C.; Pilenga, A.; Pfrang, A.; Tsotridis, G. J. *Catal.* **2009**, *265*, 199–208.
- (32) Koper, M. T. M.; Shubina, T. E.; van Santen, R. A. *J. Phys. Chem. B* **2002**, *106*, 686–692.
- (33) Yajima, T.; Uchida, H.; Watanabe, M. *J. Phys. Chem. B* **2004**, *108*, 2654–2659.
- (34) Liang, Y. M.; Zhang, H. M.; Zhong, H. X.; Zhu, X. B.; Tian, Z. Q.; Xu, D. Y.; Yi, B. L. *J. Catal.* **2006**, *238*, 468–476.
- (35) Hwang, B. J.; Sarma, L. S.; Chen, J. M.; Chen, C. H.; Shih, S. C.; Wang, G. R.; Liu, D. G.; Lee, J. F.; Tang, M. T. *J. Am. Chem. Soc.* **2005**, *127*, 11140–11145.
- (36) Lai, F. J.; Chou, H. L.; Sarma, L. S.; Wang, D. Y.; Lin, Y. C.; Lee, J. F.; Hwang, B. J.; Chen, C. C. *Nanoscale* **2010**, *2*, 573–581.
- (37) Lai, F. J.; Sarma, L. S.; Chou, H. L.; Liu, D. G.; Hsieh, C. A.; Lee, J. F.; Hwang, B. J. *J. Phys. Chem. C* **2009**, *113*, 12674.
- (38) Taufany, F.; Pan, C. J.; Chou, H. L.; Rick, J.; Chen, Y. S.; Liu, D. G.; Lee, J. F.; Tang, M. T.; Hwang, B. J. *Chem.-Eur. J.* **2011**, *17*, 10723.
- (39) Hwang, B. J.; Sarma, L. S.; Chen, C. H.; Bock, C.; Lai, F. J.; Chang, S. H.; Yen, S. C.; Liu, D. G.; Sheu, H. S.; Lee, J. F. *J. Phys. Chem. C* **2008**, *112*, 19922–19929.
- (40) Alayoglu, S.; Nilekar, A. U.; Mavrikakis, M.; Eichhorn, B. *Nat. Mater.* **2008**, *7*, 333.
- (41) Lai, F. J.; Su, W. N.; Sarma, L. S.; Liu, D. G.; Hsieh, C. A.; Lee, J. F.; Hwang, B. J. *Chem.-Eur. J.* **2010**, *16*, 4602.
- (42) Liu, S. H.; Yu, W. Y.; Chen, C. H.; Lo, A. Y.; Hwang, B. J.; Chien, S. H.; Liu, S. B. *Chem. Mater.* **2008**, *20*, 1622–1628.
- (43) Toshima, N.; Yonezawa, T. *New J. Chem.* **1998**, *22*, 1179.
- (44) Hwang, B. J.; Sarma, L. S.; Wang, G. R.; Chen, C. H.; Liu, D. G.; Sheu, H. S.; Lee, J. F. *Chem.-Eur. J.* **2007**, *13*, 6255–6264.
- (45) Koh, S.; Strasser, P. *J. Am. Chem. Soc.* **2007**, *129*, 12624.
- (46) Stern, E. A.; Newville, M.; Ravel, B.; Haskel, D. *Physica B* **1995**, *117*, 208–209.
- (47) Henkelman, G.; Arnaldsson, A.; Jonsson, H. *Comput. Mater. Sci.* **2006**, *36*, 354–360.
- (48) Sanville, E.; Kenny, S. D.; Smith, R.; Henkelman, G. J. *Comput. Chem.* **2007**, *28*, 899–908.
- (49) Dupont, C.; Hugnet, Y.; Loffreda, D. J. *J. Am. Chem. Soc.* **2006**, *128*, 9129.
- (50) Lin, Y. C.; Chou, H. L.; Tsai, M. C.; Hwang, B. J.; Sarma, L. S.; Lee, Y. C.; Chen, C. I. *J. Phys. Chem. C* **2009**, *113*, 9197.
- (51) Stamenkovic, V. R.; Mun, B. S.; Arenz, M.; Mayrhofer, K. J. J.; Lucas, C. A.; Wang, G. F.; Ross, P. N.; Markovic, N. M. *Nat. Mater.* **2007**, *6*, 241–247.
- (52) Fu, Q.; Li, W. X.; Yao, Y. X.; Liu, H. Y.; Su, H. Y.; Ma, D.; Gu, X. K.; Chen, L. M.; Wang, Z.; Zhang, H.; Wang, B.; Bao, X. H. *Science* **2010**, *328*, 1141.
- (53) Hirschl, R.; Delbecq, F.; Sautet, P.; Hafner, J. *Phys. Rev. B* **2002**, *66*, 155438.
- (54) Delbecq, F. *Surf. Sci.* **1997**, *389*, L1131.
- (55) Rodriguez, J. A.; Truong, C. M.; Goodman, D. W. *J. Chem. Phys.* **1992**, *96*, 7814.
- (56) Chen, A. C.; Holt-Hindle, P. *Chem. Rev.* **2010**, *110*, 3767.